

Field Effect Transport and Trapping in Regioregular Polythiophene Nanofibers

Jeffrey A. Merlo and C. Daniel Frisbie*

Department of Chemical Engineering and Materials Science, University of Minnesota,
421 Washington Avenue SE, Minneapolis, Minnesota, 55455

Received: July 6, 2004; In Final Form: September 3, 2004

We report the electrical characterization of field effect transistors based on regioregular poly(3-hexylthiophene) (RRP3HT) nanofibers fabricated using nanostencil shadow masks. Mobility values were $0.02 \text{ cm}^2/\text{Vs}$ with on/off current ratios of 10^6 . Current densities of $\sim 700 \text{ A/cm}^2$ were achieved in single nanofibers. A series of Soxhlet extractions was employed to separate RRP3HT into narrow molecular weight fractions. Nanofibers made from the THF fraction exhibited superior electrical properties in terms of increased current levels and decreased activation energy. The lowest activation energies in the nanofibers were achieved by using top contacts (i.e., vapor-deposited metal on top of the nanofibers) and material purified by Soxhlet extraction. Contact effects were eliminated from bottom contact devices (i.e., nanofibers on top of metal electrodes on a dielectric substrate) with a four-probe geometry. Temperature-dependent measurements reveal two distinct regimes of transport. The high-temperature regime (355–245 K) is characterized by activation energies of 62–145 meV depending on contact geometry and RRP3HT purity with a Meyer–Neldel energy of $33 \pm 3 \text{ meV}$. The low-temperature regime (235–85 K) has lower activation energies of 31–112 meV. Shifts in the turn-on gate voltage with temperature indicate $\sim 4.8 \times 10^{12}$ acceptor-like states/cm² (or ~ 1 per nm of fiber length) and 3.2×10^{12} donor-like states/cm² exist in the nanofibers. We propose that transport can be explained in terms of the multiple trap and release (MTR) or variable range hopping (VRH) formalisms of transport in a bimodal, exponential distribution of shallow and deep donor-like states.

1. Introduction

Studies of electronic transport in semiconducting polymers^{1–5} and organic semiconductors^{6–9} on the submicron scale have increased recently. There have been several reports on the fiber morphology of various conducting polymers.^{10–14} Examining electrical transport in well-defined nanostructures provides a way to investigate transport mechanisms, address the role of microstructure, and increase understanding of conduction phenomena in thin films. Nanostructures of regioregular poly(3-hexylthiophene) (RRP3HT) in the form of nanofibers^{15,16} and one-dimensional aggregates^{17,18} have been reported. Recent studies on the nanofibers using grazing incidence X-ray diffraction have demonstrated crystallinity in the nanofibers.^{19,20} The polymer chains pack in lamellar sheets perpendicular to the nanofiber axis as shown in Figure 1. The structure of the nanofibers is identical to the crystalline microdomains seen in thin films of RRP3HT.^{21,22} In fact, there have been reports of nanofiber domains observed by AFM within cast and spun-coat films of RRP3HT.^{23,24} Thus, the nanofibers represent a semi-crystalline nanostructure useful for gaining further insight into transport mechanism and bottlenecks to transport in polymer semiconductor thin films.

Crucial to investigations of the electrical properties on the nanoscale are methods to make electrical contact. Traditionally, contacts are made using e-beam lithography to define “bottom contacts” upon which the material is deposited or grown. The bottom contact geometry has been repeatedly shown to have large contact resistance for organic semiconductor and semiconducting polymer systems.^{25–27} The short channel lengths used in characterizing nanostructures exacerbate the role of the

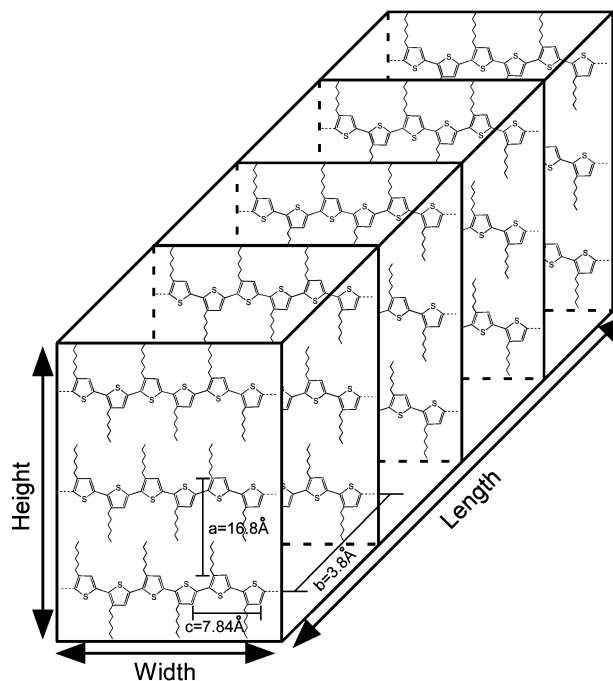


Figure 1. Schematic diagram of the nanofiber structure on the basis of GIXD studies^{19,20} and TEM/XRD study.¹⁵ The dimensions of the crystalline unit cell are indicated on the diagram. The relative dimensions are not drawn to scale. The lack of interdigitation of the hexyl chains is only schematic as there is still disagreement on the degree of interdigitation for RRP3HT. On the basis of our measurements of the nanofiber morphology, typical heights of 3–7 nm correspond to 2–4 thiophene chains; typical widths of 15 nm correspond to ~ 40 thiophene repeats; and lengths of 200 nm–5 μm correspond to ~ 500 –13 000 lamellar sheet repeats in a nanofiber.

* Corresponding author. E-mail: frisbie@cems.umn.edu.

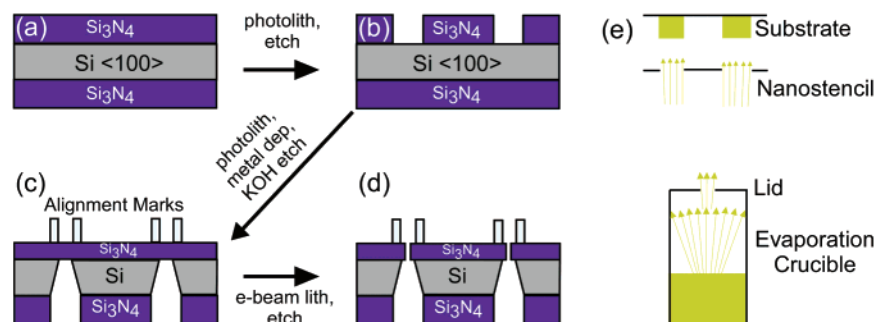


Figure 2. Schematic of nanostencil fabrication and metal deposition. (a) Low-stress silicon nitride is deposited on a silicon wafer. (b) The nitride is patterned by photolithography to expose the silicon for etching. (c) Metal alignment marks are deposited so the membranes can be located in the e-beam lithography system. The silicon is etched with KOH to release the nitride membranes. (d) The nitride is patterned with e-beam lithography and etched through. (e) Collimated evaporation of metal atoms through the nanostencil and onto the substrate.

contacts and may result in contact limited transport. Previous work has shown the top contact geometry has lower contact resistance than the corresponding bottom contact devices.^{28,29} Unlike carbon nanotubes or most inorganic systems, organic and polymeric semiconductors are not compatible with traditional resist processing that would allow lithographic patterning of top contacts. Over the past decade, procedures have been developed to pattern thin silicon nitride stencils with features down to 10 nm.³⁰ These shadow masks (nanostencils) provide a resistless method for making top contacts to organic semiconductor nanostructures.

We report here on the use of nanostencils to make top contact field effect transistors based on nanofibers of RRP3HT. These measurements are among the first to use nanostencils to characterize organic semiconductors.^{11,31} Charge transport was investigated on webs and single nanofibers of RRP3HT. The contact resistance of bottom contact transistors was examined using a four-probe method. The effect of material purity was investigated by separating commercially available material into narrow molecular weight fractions. Temperature-dependent transport measurements were performed to shed light on the conduction mechanism and trapping within the nanofibers. The effect of substrate surface energy (hydrophilic versus hydrophobic) on transport in the nanofibers was also studied.

2. Experimental Methods

2.A. Test Structure Preparation. **2.A.1. Nanostencil Shadow Masks.** The silicon nitride shadow masks (nanostencils) were fabricated following procedures reported elsewhere by several groups.^{30,32–35} The fabrication process is shown schematically in Figure 2a–d. Double-side polished (100) silicon wafers, 381- μm thick, from Virginia Semiconductor, served as the starting substrate for mask fabrication. The wafers were cleaned using the standard RCA clean sequence: 5:1:1 $\text{H}_2\text{O}:\text{NH}_4\text{OH}:\text{H}_2\text{O}_2$ at 80 °C for 15 min, 10:1 buffered oxide etch for 15 s, 6:1:1 $\text{H}_2\text{O}:\text{HCl}:\text{H}_2\text{O}_2$ at 80 °C for 15 min with a thorough deionized water rinse between each step. A 300-nm low-stress silicon nitride film was grown on both sides of the wafers by low-pressure chemical vapor deposition (100:18 sccm $\text{SiH}_2\text{Cl}_2:\text{NH}_3$, 300 mTorr, 833 °C) at a rate of 5.3 nm/min. An excess thickness of silicon nitride was used to ease wafer handling during fabrication and account for some loss of thickness during KOH etching. After aligning to the wafer flat, photolithography was used to pattern squares for the membranes and mask boundaries on the front of the wafer. These patterns were etched through the silicon nitride to the silicon beneath using a CF_4/O_2 reactive ion etch. The patterned mask boundaries become v-grooves to facilitate cleaving of the wafer into individual 8 mm \times 8 mm

masks.³⁶ The grooves were designed to etch $\sim 95\ \mu\text{m}$ into the wafer to ease cleaving but maintain wafer integrity.

After front-to-back alignment to the exposed silicon squares, photolithography was used to pattern alignment marks for use in the subsequent electron beam lithography. Before depositing $\text{Ti}(100\ \text{\AA})/\text{Pt}(1000\ \text{\AA})$, the silicon nitride was etched to 500 \AA with a CF_4/O_2 reactive ion etch. The wafers were immersed in a 45 wt % KOH bath at 80 °C ($\sim 9\ \text{h}$) to anisotropically etch the exposed silicon. The low-stress nitride serves as an effective mask to KOH and etches $\sim 7\ \text{\AA}/\text{h}$. The suspended nitride membranes are $500\ \mu\text{m} \times 500\ \mu\text{m}$. A 5-min isotropic silicon etch, $\text{HNO}_3:\text{HF}:\text{H}_2\text{O}$ 150:8:75, was used to smooth any sharp Si edges to improve the stability of the nitride membranes.³⁷ The silicon nitride was thinned to 500 \AA with a reactive ion etch before $\sim 1300\ \text{\AA}$ of 950 K poly(methyl methacrylate) was spun onto the wafer. The wafer was attached to a dummy wafer during spin coating to prevent the vacuum chuck from rupturing the fragile nitride membranes.

Source/drain patterns and alignment marks were written with a Raith 150 e-beam lithography system (20 kV, 285 $\mu\text{C}/\text{cm}^2$). The patterns were etched through the nitride membrane with a reactive ion etch (30 sccm CHF_3 , 1 sccm O_2 , 30 mTorr, 0.25W/ cm^2) following the recipe of Ralls.³⁸ The PMMA was stripped by etching in O_2 plasma.

2.A.2. Thin Oxide Substrate for Top Contacts. Substrate fabrication began with heavily doped p-type silicon wafers (Silicon Valley Microelectronics) with 3000 \AA of thermally grown silicon dioxide. The thermal oxide served as the field oxide to prevent device shorts. The oxide in the transistor region ($100\ \mu\text{m} \times 100\ \mu\text{m}$) was defined with photolithography. Reactive ion etching (CHF_3/O_2) was employed to etch down to $\sim 500\ \text{\AA}$ of SiO_2 . Buffered oxide etching removed the remaining silicon dioxide. The combination etch avoided two problems. Plasma etching the entire thickness of SiO_2 damages the silicon, which leads to a rough oxide surface during subsequent oxidation. Since the buffered oxide etch is isotropic, the etchant can bleed under the photoresist resulting in poor pattern transfer. The wafers were cleaned in piranha solution (5:1 $\text{H}_2\text{SO}_4:\text{H}_2\text{O}_2$) for 10 min to remove any traces of photoresist before oxidation. A gate oxide of 50–80 nm was grown in a dry oxidation process at 1000 °C.

Silicon dioxide on the backside of the wafer was removed with buffered oxide etch to enable electrical contact with the silicon. Ohmic contact to the silicon was made by depositing $\text{Al}(100\ \text{\AA})/\text{Au}(750\ \text{\AA})$ followed by rapid thermal annealing at 450 °C. Photolithography was used to define the contact pads that were aligned to the gate oxide as seen in Figure 3a. To enable step height coverage between the field and gate oxide,

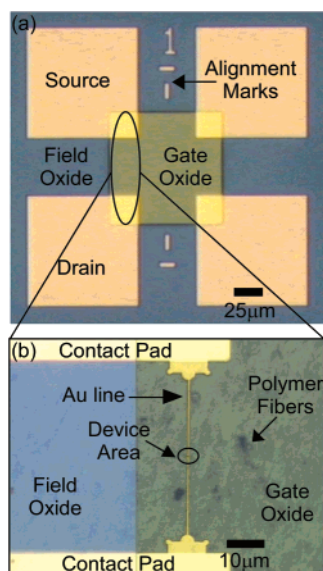


Figure 3. (a) Optical micrograph of a top contact substrate showing contact pads, alignment marks for nanostencil registration, field oxide, and gate oxide. (b) Optical micrograph of completed nanofiber transistor showing registry of nanostencil to source and drain contact pads.

70 Å Ti and 315 Å Au were deposited by a conformal electron beam evaporation. The wafers were rotated on a planetary stage during deposition. Liftoff was accomplished by dissolving the resist in acetone. The substrates were cleaned with a cycle of sonication in acetone for 10 min followed by ashing in O_2 plasma for 2 min. Some of the substrates were treated with hexamethyldisilazane (HMDS) by exposing the chips to saturated HMDS vapor for several min. Figure 3b shows an optical micrograph of a completed device with gold electrodes that were evaporated through a nanostencil onto the RRP3HT nanofibers.

2.A.3. Bottom Contact Substrate. These substrates were fabricated as described previously.³⁹ The contact geometry is four-probe with channel widths of 2 μm and lengths of 1 μm. Devices were made on bare SiO_2 and HMDS-treated SiO_2 .

2.B. Molecular Weight Fractionation. Poly(3-hexylthiophene) (regioregular, >98.5% head-to-tail) was purchased from Aldrich. The polymer was separated into narrow molecular weight fractions following the method of Trzandel et al.⁴⁰ The as-received material was subjected to a series of Soxhlet extractions with acetone, hexane, methylene chloride, and tetrahydrofuran. All the material was soluble in one of the four solvents so a chloroform extraction was unnecessary. The Soxhlet apparatus was kept under a nitrogen purge to avoid unintentional doping of RRP3HT. Each solvent was refluxed until the filtrate was colorless (~12 h). The collected fractions were concentrated by rotoevaporation and then dried until reaching constant mass.

The molecular weight and polydispersity of each fraction were characterized by matrix-assisted laser desorption ionization time-of-flight (MALDI-TOF) and gel permeation chromatography (GPC). MALDI-TOF samples were run on a Bruker Reflex III. The spectra were gathered in linear ion mode. The samples were irradiated with 4-ns pulses from a 337-nm nitrogen laser under high vacuum conditions. The accelerating voltage was 20 kV with a low mass gate of 500 Da. Each polymer fraction was dissolved in THF at a concentration of $\sim 10^{-4}$ M. The matrix dithranol was dissolved in THF at a concentration of 0.1 M. Equal volumes of the two solutions were added together before spotting the sample plate.

GPC samples were run on a Waters system with a 717 Plus autosampler, 590 HPLC pump, and a 410 differential refrac-

tometer. The samples passed through three Phenogel columns with 500, 1000, and 10000 Å pore sizes. The eluent was HPLC grade THF at 25 °C with a flow rate of 1.0 mL/min. RRP3HT solutions (~ 1 mg/mL) were 0.2 μm PTFE filtered before injection into the system. The instrument was calibrated with two sets of narrow polystyrene standards.

2.C. Solution Preparation and Nanofiber Deposition. Solutions of Aldrich RRP3HT were made as described previously.³⁹ The nanofibers precipitate from solvents with strong temperature-dependent solubility.^{15,16} The hexane, methylene chloride, and THF fractions were used to make solutions in the same manner. Upon cooling, precipitation of nanofibers was only observed for the THF fraction that dissolved in *p*-xylene when heated to 50–75 °C. The lighter fractions, hexane and methylene chloride, dissolved in *p*-xylene at room temperature and nanofibers did not precipitate from solution.

Bottom and top contact substrates were immersed in dilute solutions of Aldrich RRP3HT and the THF fraction RRP3HT to deposit nanofibers on the surface. Immersion times were typically one min, utilizing a ~ 0.05 wt % solution for webs of nanofibers and a 10:1 dilution for isolated nanofibers. All casting was done in an argon glovebox with ppm oxygen and water content to minimize doping. Samples were imaged in air with a Digital Instruments Dimension 3100 AFM in tapping mode with Si cantilevers (MicroMasch). After imaging, the bottom contact devices were placed under vacuum for electrical characterization. The top contact substrates were placed under vacuum (10^{-6} Torr) to remove any residual solvent before metal deposition.

The top contact substrates with nanofibers were loaded into a custom alignment stage to be placed in registration with a nanostencil shadow mask. The top contact substrate was held via vacuum on an *x*, *y*, *z*, θ stage (Melles Griot) with the nanostencil suspended above it with a second vacuum chuck. A zoom microscope (Navitar UltraZoom 12×) was used to look through the transparent nitride mask to place the mask and substrate into alignment via the marks seen in Figure 3a with an accuracy of ± 1 μm. After alignment, the mask and substrate were placed into contact and clamped together. The substrate stage was placed into a metal evaporator for contact deposition. Gold (500 Å) was evaporated from a Radak II furnace covered by an alumina lid with a 6-mm hole in the center to collimate the evaporated atoms. The furnace to substrate throw was 35 cm. Collimation and a long throw are essential for achieving faithful pattern transfer of submicron features as shown schematically in Figure 2e.

2.D. Electrical Characterization. Electrical characterization was performed under vacuum in ambient light using a Desert Cryogenics probe station with a base pressure of 5×10^{-7} Torr. Temperature was controlled via a Lakeshore L-331 controller between 85 and 400 K. Source and drain voltages were applied with a Keithley 236 and Keithley 237 source measure unit, respectively. Gate voltages were applied with a Keithley 6517A electrometer. Channel voltages were sensed with a pair of Keithley 6517A electrometers in four-probe measurements. Source and drain currents were independently monitored by the 236 and 237, respectively, to evaluate potential leaks in the devices. All four units shared a common ground and had an input impedance of 10^{14} Ω. All leads except the gate used triaxial cables with the electrometers run in guarded mode to minimize electrical noise and leakage currents.

Linear mobility was calculated using the transconductance (g_m) at a specific drain voltage. The turn-on voltage (V_0) was determined as the onset of exponential current increase from a

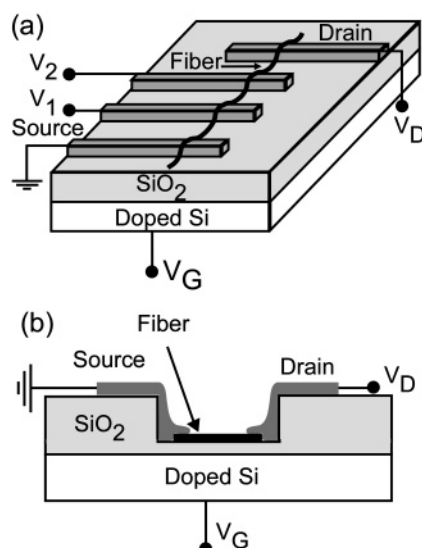


Figure 4. (a) Schematic of a bottom contact nanofiber transistor. The nanofibers are deposited on top of the four electrodes. The four-probe geometry is used to eliminate contact resistance effects. (b) Cross-sectional schematic of a top contact nanofiber transistor with a thin gate oxide and thick field oxide.

TABLE 1: Summary of RRP3HT Molecular Weight Fractions Obtained by Soxhlet Extraction

fraction	wt%	MALDI-TOF			GPC		
		M_n^a	M_w^a	PDI ^a	M_n	M_w	PDI
Aldrich					46600	92700	1.99
Acetone	0.1				4200	7300	1.74
Hexane	1.2	2754	3205	1.16	5400	7900	1.46
CHCl ₃	30.3	5341	5790	1.08	10600	14800	1.40
THF	68.4	6586	7232	1.10	14300	21400	1.49

^a M_n denotes the number-average molecular weight (g/mol), M_w denotes the mass-average molecular weight (g/mol), and PDI is the polydispersity index.

logarithmic plot of drain current ($\log I_D$) versus gate voltage (V_G). I_D - V_G sweeps were taken in 1.0 V gate steps from +50 V to -100 V back to +50 V for devices with a SiO₂ thickness of 2830 Å and from +30 V to -35 V back to +30 V for devices with 805 Å of oxide. Typical sweeps took 6.5 and 2 min, respectively, for each drain voltage. I_D - V_D sweeps were taken in 0.5 V drain steps from 0 V to -10 V back to 0 V for all devices. Typical sweeps took 45 s for each gate voltage. The geometries of the top and bottom contact nanofiber devices are shown in Figure 4.

3. Results and Discussion

3.A. Molecular Weight Fractionation. The results of the separation of Aldrich RRP3HT into narrow molecular weight fractions are shown in Table 1. The starting material from Aldrich had a large polydispersity and molecular weight as can be seen from the GPC results. These results are consistent with those reported elsewhere in the literature^{23,41,42} and with the value ($M_w = 87\,000$ g/mol) given by Aldrich. MALDI-TOF has low signal intensity for large molecular weights and is inaccurate for polydispersity values above 1.2 so the Aldrich RRP3HT was not analyzed by this technique.⁴³⁻⁴⁶

The series of consecutive Soxhlet extractions divided the Aldrich RRP3HT into three narrow molecular weight fractions plus a very small acetone fraction (<1 mg) of low molecular weight components and impurities. The majority of the material was extracted in the THF fraction. These results are consistent

with other fractionations of RRP3HT.^{40,41} The starting material and all fractions except the acetone fraction were shiny and green. The acetone fraction was orange/red in color and likely contained most of the residual metal salts from polymerization and low molecular weight oligothiophenes. Recent studies of the chemical purity of Aldrich RRP3HT reveal a significant amount of residual Zn and Br from the polymerization.^{47,48} GPC analysis showed the acetone fraction still had a large polydispersity and did contain the lowest molecular weight components. When referenced to polystyrene standards, GPC tends to overestimate the molecular weight by a factor of 2 in agreement with other reports in the literature^{41,49} and the MALDI-TOF data presented here.

Transistors made with nanofibers from the THF fraction exhibited superior performance in comparison to identically prepared devices using Aldrich material. Current levels were typically a factor of 2–3 higher in devices made from the THF fraction nanofibers. Other groups have seen improved reproducibility and performance in diodes and transistors made from fractionated RRP3HT.^{50,51} We believe that the performance improvement is not due to a specific dependence on molecular weight but rather is the result of removing residual impurities from polymerization. The reduced activation energy (see Temperature Dependence, 3.D.) indicating fewer or shallower traps supports this conclusion.

3.B. Top Contact Transport Measurements. *3.B.1. Nanofiber Webs.* Figure 5a shows an AFM image of a typical top contact nanofiber web transistor. The Au electrodes define a nominal channel width of 2 μm with a channel length of 500 nm. The nominal W/L ratio is modified to account for the coverage of nanofibers in the channel for mobility calculations. The I_D - V_G characteristics of this device are shown in Figure 5b for two different V_D values for the forward and reverse gate voltage sweeps. From the negative gate voltages used to achieve maximum conductivity, it is clear that the nanofibers are hole conductors. The on/off current ratio is $\sim 10^6$ and the mobility estimated from the transconductance in the linear regime of the forward sweep is 0.02 cm²/Vs. The mobility value is slightly lower than the value reported for a device with aligned RRP3HT nanofibers.⁵²

The hysteresis exhibited between the forward and reverse sweeps in Figure 5b is indicative of trapping in the nanofibers. The shift of the turn-on voltage for the I_D - V_G traces at different drain voltages is a bias stress effect also due to trapping. Figure 5c shows the I_D - V_D curves for the same device. Hysteresis in I_D - V_D sweeps is less than in I_D - V_G traces which is due to the respective voltage being swept. Trapping effects are emphasized in an I_D - V_G measurement since the gate voltage (i.e., charge carrier concentration) is continuously varied. An I_D - V_G sweep is a dynamic measurement with respect to charge trapping since the semiconductor is being driven away from equilibrium by the rapidly varying charge carrier concentration (~ 1 s per gate volt step). In other words, the increase in the number of carriers from additional gate voltage on the forward sweep masks the effect of charges being trapped until the sweep direction is reversed. On the other hand, an I_D - V_D measurement occurs at a fixed charge concentration while the driving force (drain voltage) is varied. During the sweep, the induced charge nearly reaches equilibrium with the trap states, and hysteresis is reduced.

Current saturation in an I_D - V_D sweep was only observed by using a sufficiently thin gate oxide to avoid short channel effects in the 500-nm length devices. Nanofiber web transistors made on bare SiO₂ and HMDS-treated SiO₂ had nearly identical

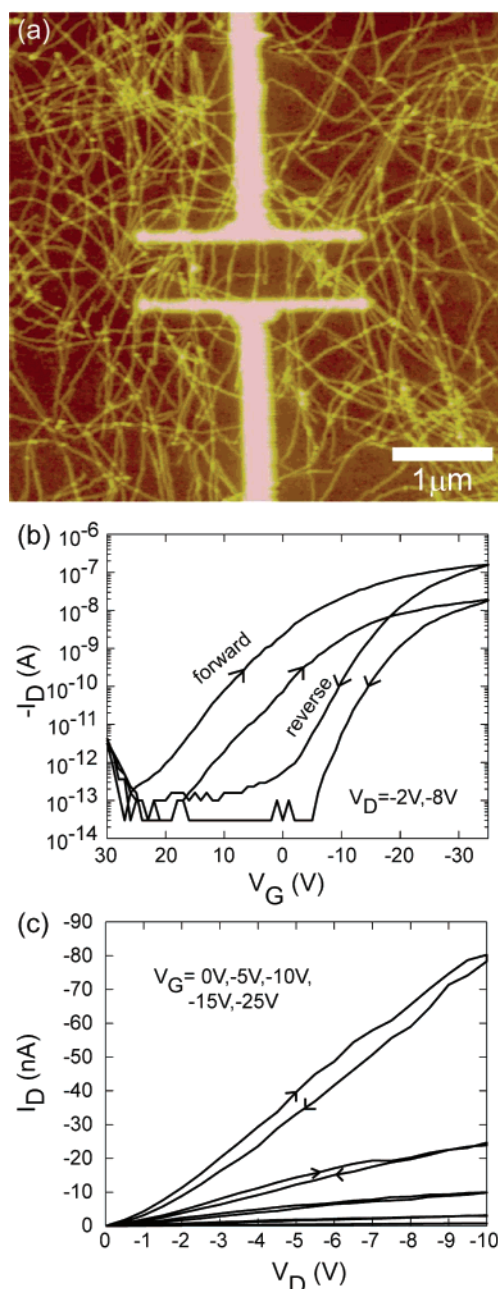


Figure 5. (a) AFM image of Au electrodes on top of RRP3HT nanofibers. (b) I_D – V_G characteristics for $V_D = -2$ V and -8 V of the top contact nanofiber web device shown in (a) at 295 K. The forward and reverse sweeps exhibit a large hysteresis because of trapping. (c) I_D – V_D curves for same device at 295 K. The gate oxide is 805 Å.

current levels and on/off current ratios at the same charge carrier density. Devices on HMDS-treated SiO_2 had turn-on voltages (V_0) closer to zero than bare SiO_2 devices. Typical room-temperature values for V_0 (805 Å SiO_2) were +20 V for bare SiO_2 and +5 V for HMDS-treated SiO_2 . The positive V_0 values could be the result of doping in the nanofibers (most likely from oxygen) or the presence of acceptor-like traps⁵³ at the interface. Exposure to air in other experiments resulted in bulk doping of the nanofibers and nonzero off currents ($\geq 10^{-9}$ A). Since the off currents of the devices studied are $\leq 10^{-13}$ A, bulk doping can be eliminated and the positive V_0 values can be attributed to acceptor-like interfacial traps. The change in V_0 with substrate surface treatment supports this conclusion. There was no clear difference in mobility and on/off current ratio on the basis of the substrate for the top contact devices. Previous results showed

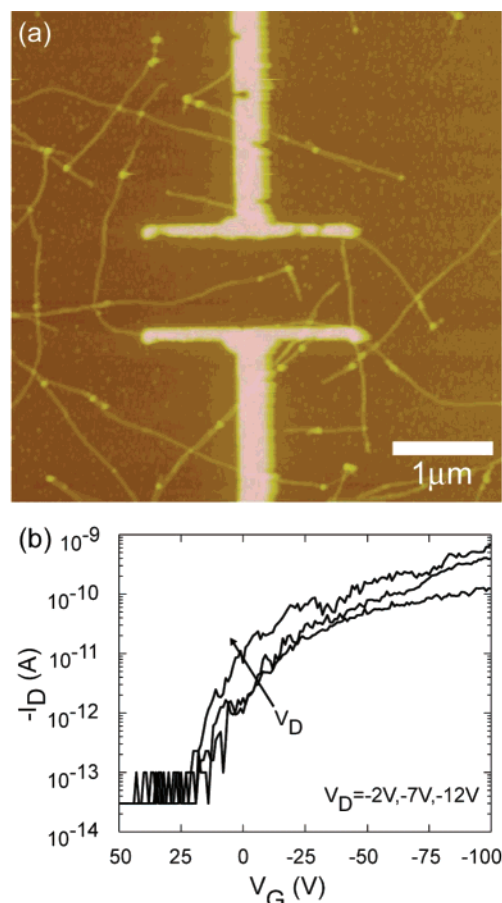


Figure 6. (a) AFM image of Au electrodes deposited on top of a single nanofiber. (b) I_D – V_G curves for $V_D = -2$ V, -7 V, and -12 V for the single nanofiber shown above. The gate oxide is 2830 Å.

enhanced current levels with HMDS-treated SiO_2 for bottom contact devices.³⁹

Control experiments were performed to assess the importance of parallel current paths between the macroscopic contact pads of our devices. Electrical tests prior to deposition of the nanoelectrodes revealed that there was a parallel current path of web conduction, but current levels were less than 5% of current levels observed in completed devices (Figure 3b). Furthermore, these parallel currents between the contact pads required very large turn-on voltages (> -70 V for 2830 Å oxide and > -20 V for 805 Å oxide). This contribution was neglected in data analysis.

3.B.2 Single Nanofibers. By casting from dilute solutions, transistors with single nanofibers were made. Figure 6a shows an image of Au electrodes on top of a single nanofiber (6.6-nm height \times 15-nm width \times 875-nm length) on HMDS-treated SiO_2 . The I_D – V_G characteristics are shown in Figure 6b. The linear mobility is calculated to be 0.007 cm^2/Vs for a nanofiber composed of Aldrich (unpurified) RRP3HT. The maximum current density for the single nanofiber was ~ 700 A/ cm^2 . The single nanofiber top contact transistors had stable turn-on voltages and did not exhibit the same level of trapping seen in bottom contact devices where large turn-on voltage shifts were observed.³⁹ This difference suggests a large number of traps were located between the embedded gold electrodes and the nanofibers in the bottom contact geometry. Hysteresis between forward and reverse traces was still observed.

3.C. Contact Resistance. The contacts to the nanofibers for the bottom contact geometry were characterized using the four-probe method that has been applied to organic semiconduc-

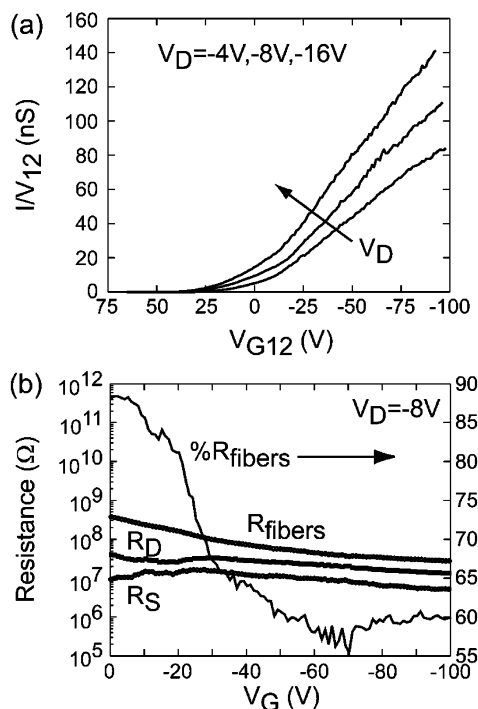


Figure 7. (a) I_D/V_{12} vs V_{G12} for $V_D = -4$ V, -8 V, and -16 V for a bottom contact device on SiO_2 with THF fraction nanofibers. (b) Plot of source, drain, and fiber resistance as a function of gate voltage on the left axis. The right axis is fiber resistance as a percentage of the total resistance. The gate oxide was 2830 Å for this device.

tors^{39,54–58} and a-Si:H.^{59–61} Two voltage-sensing electrodes (V_1 and V_2) are equally spaced within the channel (Figure 4a). These electrodes sense the potential in the channel and can be used to extract the contact resistance of the source and drain electrodes independently. The four-probe method is only valid in the linear regime of device operation where $(V_G - V_T) \gg V_D$ and the gradual channel approximation holds. On the basis of a linear extrapolation of the voltage between the sense probes, the source (ΔV_S) and drain (ΔV_D) contact voltage drops are given by

$$\Delta V_S = \frac{L_2 V_1 - L_1 V_2}{L_2 - L_1} - V_S \quad (1)$$

$$\Delta V_D = V_D - \frac{L(V_2 - V_1) + L_2 V_1 - L_1 V_2}{L_2 - L_1} \quad (2)$$

where V_S , V_D , V_1 , and V_2 are the voltages at the source electrode, drain electrode, first sense electrode, and second sense electrode, respectively, and L , L_1 , and L_2 are the distances measured from source to drain, source to the first sense electrode, and source to the second sense electrode, respectively. The corresponding contact resistances can be calculated by dividing each contact voltage drop by I_D .

In addition to calculating contact resistance, a contact-corrected mobility denoted by μ_{12} can be calculated from the modified transconductance using⁶²

$$\frac{I_D}{V_{12}} = \frac{W}{L_2 - L_1} \mu_{12} C_{\text{ox}} (V_{G12} - V_{T12}) \quad (3)$$

where I_D is the drain current, $V_{12} = V_2 - V_1$, C_{ox} is the capacitance of the oxide per unit area, $V_{G12} = V_G - (V_1 + V_2)/2$ is the effective gate field in the middle of the channel, and V_{T12} is the contact-corrected threshold voltage. Figure 7a shows a

plot of I_D/V_{12} versus V_{G12} used to determine contact-corrected mobility for three drain voltages.

Using eqs 1 and 2 to calculate voltage drops at the contacts, room-temperature values for the combined specific contact resistance were calculated to be 2–10 kΩcm for the bottom contact devices in agreement with reported literature values for Au–RRP3HT bottom contacts.^{27,63–65} The device width was calculated by taking the nominal width (2 μm) and multiplying by the percentage coverage of the nanofibers within the channel to get the effective device width. Figure 7b shows the resistance of the fibers, source contact, and drain contact as a function of gate voltage for $V_D = -8$ V. The percentage of the resistance due to the fibers is given on the same plot. For all bottom contact devices at room temperature, the drain resistance, R_D , was about a factor of 2 greater than the source resistance, R_S . Previous work by Bürgi et al. has shown nearly equal source and drain resistances for Au–RRP3HT contacts.²⁷ However, their work suggests that simple Schottky barrier models are not adequate to describe the contact resistance, and bulk transport through a narrow region by each contact may dominate as appears to be the case here. The channel resistance due to the nanofibers only makes up 60% of the total resistance at large gate voltages as seen in Figure 7b. Therefore, the contact resistance correction is necessary to examine the properties of the bottom contact nanofiber devices.

3.D. Temperature Dependence. Organic semiconductors and conducting polymers typically show activated behavior over a wide range of temperatures. Studies of RRP3HT thin films⁶⁶ have revealed gate voltage dependent activation energies of 54–57 meV,⁶⁷ 100–200 meV,⁶⁸ 60–100 meV,⁶⁹ and 100–160 meV.²⁷ Figure 8a shows the evolution of the I_D – V_G traces for a top contact nanofiber web transistor as a function of temperature. It is clear that (1) the device is on at $V_G = 0$ V at room temperature, (2) transport is activated from the decrease in drain current as temperature is decreased, and (3) the turn-on voltage (V_0) shifts negatively as temperature is decreased. Furthermore, the sharpness of the device turn-on (sharpness is inversely proportional to the subthreshold swing = $dV_G/d(\log I_D)$) first increases as the temperature is decreased until ~245 K and then decreases with further drop in temperature. These observations can be explained by the presence of both acceptor-like and donor-like state distributions. As noted earlier, the positive V_0 at high temperatures likely reflects the presence of interfacial acceptor states that produce free holes in the fibers.⁷⁰ As temperature decreases, the number of acceptor-induced holes decreases, and V_0 shifts toward zero (i.e., the device is less conductive at $V_G = 0$ V at lower temperatures because there are fewer acceptor-induced holes). The changes in the subthreshold swing with temperature and further negative shifts in V_0 are indicative of movement of the Fermi level through a *bimodal distribution* of deep and shallow donor-like states that trap holes. At high temperatures, the subthreshold swing is large because there is enough thermal energy to release the holes that are captured in deep donor-like traps so that a large distribution of donor-like trap states is sampled as the gate voltage is swept. However, as temperature decreases, less thermal energy is available to the holes and consequently a shallower distribution of donor-like trap states must be sampled. For a single monotonic distribution of traps (i.e., continuously increasing density moving toward the edge of the valence band), decreasing temperature should broaden the I_D – V_G curve that is, increase the subthreshold swing as more gate voltage is required to move the Fermi level through the trap distribution. However, initially the subthreshold swing decreases, which indicates that in a certain

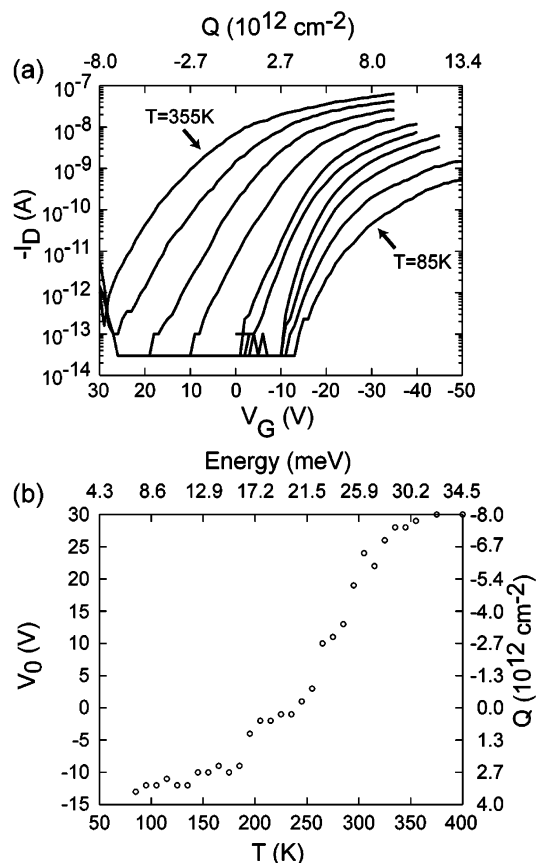


Figure 8. (a) Evolution of I_D – V_G traces as a function of temperature for a top contact nanofiber web transistor on bare SiO_2 ($V_D = -4$ V, oxide thickness = 805 Å). The traces span 355–85 K in increments of 30 K. A shift in the turn-on voltage (V_0) toward increasingly negative values is observed. To allow investigation of similar charge carrier densities, the gate-voltage sweep was increased to more negative voltages to compensate for the V_0 shift. (b) Evolution of V_0 with temperature. The SiO_2 is 805 Å for this device. The top axis is the thermal energy corresponding to the temperature on the bottom axis. The right axis is the amount of charge corresponding to V_0 .

range of temperatures it is possible to both completely fill the deep traps and for the conduction to be relatively unaffected by the shallow traps because thermal energy is comparable to the shallow trap depth. The sharpening of the I_D – V_G curve initially upon cooling indicates a nonmonotonic (bimodal) trap distribution. With still further decrease in temperature, the thermal energy becomes small enough that the residence time of the holes in the shallow donor-like traps increases leading again to a more gradual increase in current with gate voltage and increasing subthreshold swing. Further evidence for both a bimodal donor-like trap distribution and interfacial acceptor-like traps is presented below.

Figure 8b shows the shift in V_0 with temperature more clearly. We have examined several devices and there are similar shifts in V_0 when normalized to the number of charge carriers ($Q = C_{\text{ox}}V_0/e$) versus thermal energy (k_bT). Considering shifts in the turn-on voltage from positive values to zero as indicative of acceptor-like states and shifts from zero to negative V_0 values resulting from donor-like states, a rough calculation of the donor and acceptor concentrations in the nanofibers can be made. From the average of all devices tested, a slope of $5.0 \times 10^{11} \text{ cm}^{-2} \text{ meV}^{-1}$ is calculated for the change in carrier concentration for V_0 shifts between positive values and zero. Multiplying by the change in thermal energy between 355 K and 245 K (9.5 meV), $\sim 4.8 \times 10^{12} \text{ cm}^{-2}$ is calculated as the approximate number of acceptor-like states. The number of acceptors corresponds to

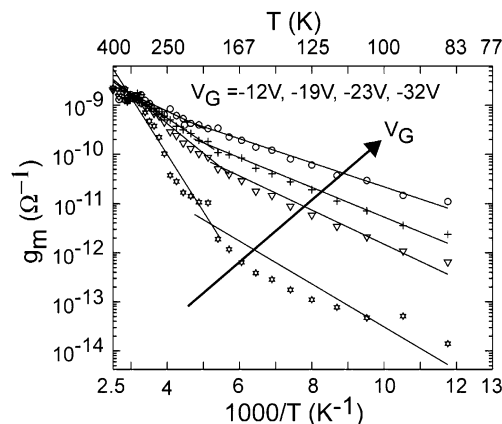


Figure 9. Transconductance as a function of inverse temperature for a typical top contact nanofiber web device illustrating two regimes of dependence. The high-temperature regime is from 355–245 K and the low-temperature regime from 235–85 K. The lines serve as a guide to the eye for illustrating the transitions between the two regimes. The transition temperature is gate-voltage dependent as can be seen from the shifting intersection point.

~ 1 per nm of fiber length or 1 per 375 thiophene repeat units on the basis of the structure shown in Figure 1. Performing the same calculation for the V_0 shift from zero to negative values yields $3.2 \times 10^{12} \text{ cm}^{-2}$ donor-like states.

An Arrhenius plot of the transconductance versus inverse temperature at different gate voltages is shown in Figure 9. Between 355 K and 245 K, a regime of higher activation energy is seen with a transition to lower activation energy below 245 K. These two regions were seen in each device independent of contact geometry, substrate surface energy, and purity of the polymer material. The transition between the two activated regimes is a function of gate voltage as can be seen from the fit lines in Figure 9. For $V_G = -12$ V, the transition is ~ 195 K while for $V_G = -32$ V, the transition is at ~ 250 K. At large gate voltages, the distinction between the two regimes nearly disappears. The reason that the two regimes are less distinct at high gate voltages is that the deep donor-like traps (which yield higher activation energies) have been filled; in this case, the carriers sample only the shallow donor-like trap states. The gate-voltage dependence of the transition temperature suggests that the presence of two distinct donor-like trap distributions in the nanofibers, rather than a phase transition at a specific temperature, is the cause of the activation energy transition. Recent work on regioregular poly(3-hexylthiophene) has suggested the existence of a double-peaked Gaussian distribution of trap states.^{71,72} Work on another regioregular polythiophene⁷³ has revealed nonmonotonic behavior of the mobility as a function of temperature similar to that observed here, also consistent with a bimodal trap distribution. The precise nature of the two distributions of donor-like trap states cannot be determined by these measurements. Since the fractionation did have a substantial effect on the number of donor-like traps within the nanofibers (discussed in the next section), some of the deeper donor-like states were due to impurities. It is likely that additional deep donor-like traps are due to a structural defect in the nanofibers, possibly the transition between the amorphous and crystalline regions or defects from less than 100% head-to-tail linkage in the polymer chains. The shallow donor-like states could be the result of so-called contact traps, that is, traps induced by structural disorder around the contacts. For the bottom contact devices, structural disorder could be introduced into the nanofibers by conforming to the topology of the contacts, while for the top contact devices the hot metal

deposited on top of the nanofibers could introduce traps at the contact/polymer interface.

Two common models for activated transport are multiple trap and release (MTR)⁷⁴ and variable range hopping (VRH).⁷⁵ MTR assumes most of the injected carriers are trapped in an exponential distribution of states in the band gap and are thermally activated to an extended transport state. MTR is able to predict gate-voltage dependent activation energy due to the Fermi level of the material moving through the distribution of states, which increases the mobility. MTR proposes that the effective mobility (μ_{eff}) is the free carrier mobility (μ_0) multiplied by the ratio of free holes (N_V) to total induced holes ($N_V + N_T$)

$$\mu_{\text{eff}} = \mu_0 \frac{N_V}{N_V + N_T} = \frac{\mu_0}{1 + \frac{N_T}{N_V}} \quad (4)$$

where N_T is the areal density of trapped holes and N_V is the areal density of free holes defined by

$$N_V = N_{V0} \exp\left(\frac{E_F - E_V}{k_B T}\right) \quad (5)$$

where N_{V0} is the effective density of states at the valence band edge (E_V), k_B is the Boltzmann constant, and E_F is the Fermi level.

To illustrate the functional form of the temperature dependence of the mobility, we assume a discrete trap state at energy E_T which yields

$$N_T = N_{T0} \exp\left(\frac{E_T - E_F}{k_B T}\right) \quad (6)$$

Combining eqs 4–6 yields the following form for the temperature dependence of the effective mobility

$$\mu_{\text{eff}} = \mu_0 \frac{1}{1 + \frac{N_{T0}}{N_{V0}} \exp\left(\frac{E_T - E_V}{k_B T}\right)} \approx \mu_0 \exp\left(\frac{-E_A}{k_B T}\right) \quad (7)$$

where E_A is the difference in energy between the discrete trap state and the valence band edge ($E_T - E_V$). Equation 7 is well approximated by a simple Arrhenius expression if $E_A \gg k_B T$ and $N_{V0} \sim N_{T0}$. Thus, the MTR model predicts activated behavior for the mobility. Since the trap distribution is more accurately modeled as an exponential distribution (eq 10), the measured activation energy is a convolution of the trap depth and distribution.

The VRH model of Vissenberg et al.⁷⁵ proposes that transport occurs via hopping in an exponential distribution of localized states. Mobility is thermally activated and follows a simple Arrhenius relationship. This prediction is different than Mott VRH where $\mu \sim \exp[-(T_0/T)^{1/3}]$ for two-dimensional hopping.⁷⁶ Mott VRH assumes hopping through a constant density of states, which leads to the different temperature dependence. The Vissenberg model predicts gate-voltage dependent mobility and activation energy similar to MTR. As the gate voltage is increased, injected carriers fill the lower energy states. Additional carriers begin to fill higher energy states, which require lower activation energy to hop to the next site. Consequently, the activation energy decreases, and the mobility increases with increasing gate voltage.

Hopping in an exponential distribution of states can also be described in terms of an effective transport level or energy.^{77,78}

Carriers are activated from the Fermi level to the transport energy. Hopping transport described in this fashion closely resembles the formalism of MTR with a single trap level. Therefore, it is difficult to distinguish between MTR and VRH in a distribution of exponential states on the basis of mobility as a function of temperature data as noted by other researchers.⁷³ In fact, both VRH^{75,79} and MTR^{69,80} have been used to describe transport in thin films of RRP3HT.

For quantities with a thermally activated behavior (and shown here specifically for the transconductance), it has been empirically found that

$$g_m = g_{m0} \exp\left(-\frac{E_A}{k_B T}\right) \quad (8)$$

and

$$g_{m0} = g_{m00} \exp\left(\frac{E_A}{E_{MN}}\right) \quad (9)$$

where g_m is the transconductance, g_{m0} is the transconductance prefactor, E_A is the activation energy, and $E_{MN} = k_B T_0$ is the Meyer–Neldel energy. In a common interpretation, the Meyer–Neldel energy represents the width of the distribution of traps or states and T_0 is called the isokinetic temperature. A Meyer–Neldel energy was observed for the high-temperature regime as is discussed in the next section. The presence of the isokinetic temperature suggests the presence of a well-defined distribution of trap states in the nanofibers. An exponential distribution of states for a p-type semiconductor is given by

$$N_T(E) = \frac{N_{T0}}{k_B T_0} \exp\left(-\frac{E - E_V}{k_B T_0}\right) \quad (10)$$

where N_{T0} is the density of traps (#/cm²), T_0 is the temperature that characterizes the width of the distribution, and E_V is the energy of the valence band edge.

3.D.1 High-Temperature Regime. Figure 10a shows a plot of transconductance versus inverse temperature for several gate voltages for a typical web device. The straight line fits are based on data between 355 K and 245 K, which yields the activation energy. The straight line fits begin to deviate from the data below 245 K (depending on gate voltage) as the activated regime changes. The different slopes of the lines represent the variation of the activation energy with gate voltage as shown in Figure 10b. The gate-voltage dependent activation energy is predicted by the MTR and VRH formalisms. All devices have the highest activation energy at low gate voltage that steadily decreases with increasing gate voltage. As can be seen in Figure 10a, the activation energy line fits intersect at ~ 350 K. This point is the isokinetic temperature (T_0), where $k_B T_0$ is the width of the trap (localized state) distribution in MTR (VRH). A semilog plot of the transconductance prefactor ($g_{m,0}$) versus activation energy is shown in Figure 10c. As discussed above, the prefactor for an activated quantity can obey the Meyer–Neldel rule. A Meyer–Neldel energy (E_{MN}) of 30 meV is determined from a linear fit to the data (using eq 9) in Figure 10c. This corresponds well to the isokinetic temperature (i.e., $k_B \cdot 350$ K = 30.2 meV ~ 30 meV) seen in Figure 10a. Meyer–Neldel behavior has been previously observed in organic semiconductors.^{58,81} All nanofiber devices tested exhibited a Meyer–Neldel energy of 33 ± 3 meV. Thus, the width of the distribution of traps (localized states) that dominates transport in the nanofibers for this range was not affected by material purity, substrate surface energy, or contact geometry. A likely origin for these traps is structural

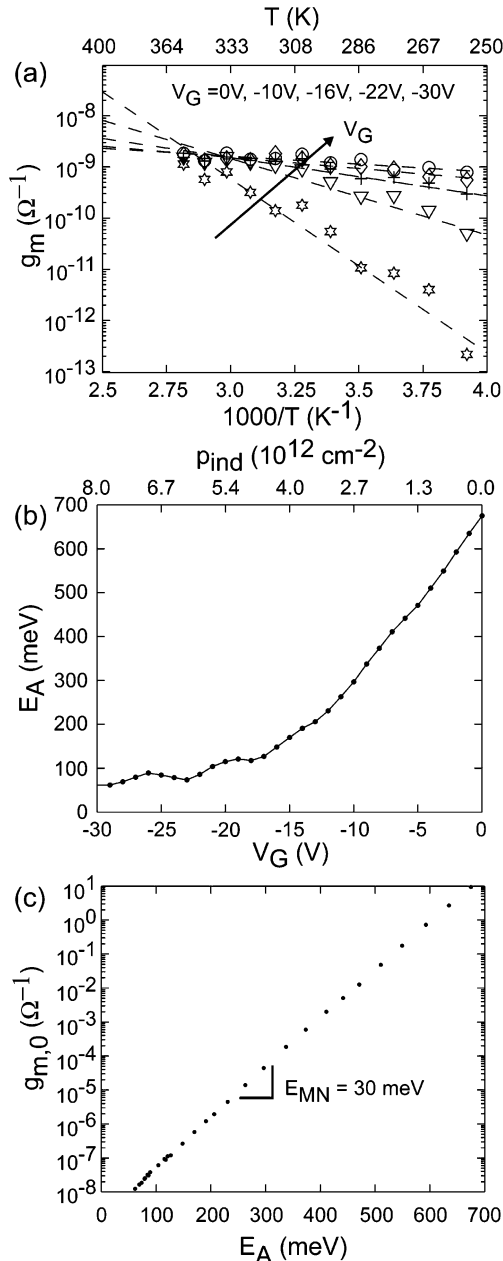


Figure 10. (a) Transconductance (g_m) vs inverse temperature for several gate voltages for the top contact device in Figure 5a. The fit lines are from 355–245 K and intersect at ~ 350 K. (b) Transconductance based activation energy vs gate voltage. (c) Transconductance prefactor ($g_{m,0}$) vs activation energy. The inverse of the slope of this line is the Meyer–Neldel energy ($E_{MN} = 30$ meV), which corresponds to an isokinetic temperature of ~ 350 K as seen in part a.

defects, possibly domain boundaries between amorphous and crystalline regions or defects from less than 100% head-to-tail linkage in the polymer chains.

Transport in the high-temperature regime between 355 K and 245 K as a function of contact geometry, material purity, and substrate surface energy is summarized in Table 2. Activation energy based on the linear (high V_G) mobility ranged from 62 to 135 meV. The clear trend is reduction of activation energy by changing from bottom to top contacts and using fractionated RRP3HT over Aldrich RRP3HT. These two factors in combination reduce the activation energy by over a factor of 2. Among the bottom contact devices, there is $\sim 10\%$ decrease in activation energy when using the THF fraction RRP3HT to precipitate the nanofibers. The surface energy of the substrate does not

TABLE 2: Summary of Activation Energy for Different Contact Geometries, Material Purity, and Substrates in the High-Temperature (355–245 K) Regime

contact geometry	substrate	material	E_A (μ) (meV) ^a	E_A (g_m) (meV) ^b	E_{MN} (meV)
bottom 4 probe	SiO ₂	Aldrich	133	145–485	31
bottom 4 probe	HMDS	Aldrich	135	235–840	33
bottom 4 probe	SiO ₂	THF fraction	127	147–860	35
bottom 4 probe	HMDS	THF fraction	117	162–670	35
top 2 probe	HMDS	Aldrich	100	110–500	31
top 2 probe	SiO ₂	THF fraction	62	40–350	30
top 2 probe	HMDS	THF fraction	63	65–650	32

^a Mobility values were calculated on the basis of the transconductance in the linear regime of transistor operation at high gate voltage ($(V_G - V_T) \gg V_D$) for two-probe devices. For four-probe devices, the mobility was calculated using the modified transconductance method described previously. ^b Activation energy as a function of gate voltage is based on the transconductance for two-probe devices and modified transconductance for four-probe devices (see Figure 10b). Activation energy and mobility are calculated at an electric field of 8×10^4 V/cm.

appear to have a significant effect on the activation energy for top contact devices. All devices exhibit activation energy with a strong gate-voltage dependence.

The higher activation energies seen in the bottom contact data support the interpretation that some traps are associated with the contacts. The traps in the bottom contact geometry are possibly due to the nanofiber adapting to the topography of the contacts on the surface. The bending and kinking of the nanofibers likely introduces structural disorder that results in traps near the contacts.

3.D.2. Low-Temperature Regime. Transport in the low-temperature regime between 235 K and 85 K is characterized by lower activation energy in comparison to the high-temperature regime. Similar transitions between activated regimes have been observed in a-Si:H.⁸² Figure 11a shows a plot of transconductance versus inverse temperature for several gate voltages for the low-temperature region (fits based on data between 235 K and 85 K) for a top contact web device. The lines shown are fits to the basic Arrhenius Equation. The variation of activation energy with gate voltage is shown in Figure 11b. Attempts to fit the data in this temperature range to a VRH model ($\mu \sim \exp[-(T_0/T)^{1/3}]$) did not yield an improved fit to the data. The full data set is summarized in Table 3 for the same devices as Table 2 for the low-temperature region. All top contact devices were characterized down to 85 K and still passed detectable current. Bottom contact devices made with Aldrich RRP3HT passed current until 155 K and THF fraction RRP3HT devices conducted until 115 K. These results reflect room-temperature current levels and the relative activation energies of the various devices.

The trends in activation energy for the low-temperature regime are similar to those in the high-temperature regime. However, for the bottom contact devices a large variance is seen on the basis of material purity and substrate. Using the THF fraction material clearly reduces the activation energy. The activation energy also exhibits a dependence on the substrate, HMDS-treated or bare SiO₂, for bottom contact devices. In Aldrich RRP3HT, the activation energy is reduced by nearly a factor of 2 when switching from SiO₂ to HMDS-treated SiO₂. Again, top contacts with the THF fraction material resulted in the lowest activation energy. The activation energies in this regime are indicative of the shallow donor-like traps in the nanofibers.

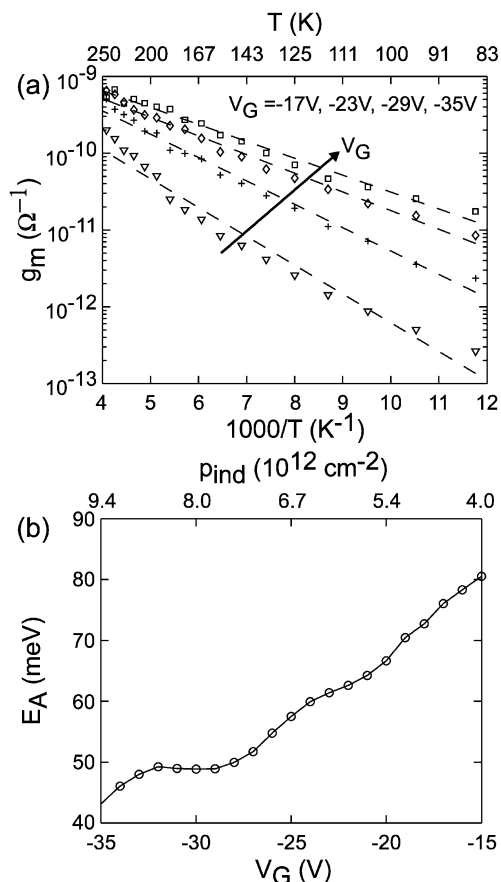


Figure 11. (a) g_m vs $1/T$ for the low-temperature regime (235–85 K) for the top contact device in Figure 5a. (b) Activation energy vs gate voltage for the low-temperature regime.

TABLE 3: Summary of Activation Energy for Different Contact Geometries, Material Purity, and Substrates in the Low-Temperature (235–85 K) Regime

contact geometry	substrate	material	E_A (μ) (meV)	E_A (g_m) (meV)
bottom 4 probe	SiO ₂	Aldrich	112	100–185
bottom 4 probe	HMDS	Aldrich	68	50–300
bottom 4 probe	SiO ₂	THF fraction	52	45–75
bottom 4 probe	HMDS	THF fraction	41	45–75
top 2 probe	HMDS	Aldrich	43	35–80
top 2 probe	SiO ₂	THF fraction	31	40–85
top 2 probe	HMDS	THF fraction	34	40–80

4. Conclusions

We have reported on field effect transistors of RRP3HT nanofibers fabricated through the use of nanostencil shadow masks. Mobility values were as high as $0.02 \text{ cm}^2/\text{Vs}$ with on/off current ratios of 10^6 . Aldrich RRP3HT fractionated by a series of Soxhlet extractions yielded transistors with increased current levels and reduced activation energy. Four-probe measurements reveal a specific contact resistance of 2–10 $k\Omega\text{cm}$ for bottom contact devices. Variable temperature measurements reveal two distinct regimes of activated transport, which strongly suggest a bimodal distribution of deep and shallow donor-like trap states. Positive turn-on voltage values also indicate the presence of interfacial acceptor-like trap states. A high-temperature regime (corresponding to the deep donor-like traps) is characterized by mobility activation energies of 62–145 meV with a Meyer–Neldel energy of 33 ± 3 meV. The Meyer–Neldel energy corresponds to the observed isokinetic point of 350 K. The low-temperature regime (shallow donor-like traps) has reduced mobility activation energies of

31–112 meV. Activation energy in both regimes exhibited strong gate-voltage dependence. The lowest activation energies were observed in devices with nanofibers made from the THF fraction using top contacts. The data in both temperature regimes are consistent with either the MTR or VRH formalism of transport in an exponential distribution of states. Our measurements demonstrate that probing nanostructures may allow clearer examination of the effect of traps on transport.

Acknowledgment. The authors thank C. R. Newman for writing the MATLAB code for data analysis and R. J. Chesterfield and P. V. Pesavento for helpful discussions and equipment support. This work was supported in part by the American Chemical Society Petroleum Research Fund (36589-AC) and the Materials Research Science and Engineering Center at Minnesota (DMR-021302), which is funded by the National Science Foundation. C.D.F. also acknowledges financial support from 3M Company.

References and Notes

- (1) Austin, M. D.; Chou, S. Y. *Appl. Phys. Lett.* **2002**, *81*, 4431.
- (2) Hamadani, B. H.; Natelson, D. *Mater. Res. Soc. Symp. Proc.* **2003**, *771*, 187.
- (3) Hamadani, B. H.; Natelson, D. *Appl. Phys. Lett.* **2004**, *84*, 443.
- (4) Hamadani, B. H.; Natelson, D. *J. Appl. Phys.* **2004**, *95*, 1227.
- (5) Xu, Y.; Berger, P. R. J. *Appl. Phys.* **2004**, *95*, 1497.
- (6) Zhang, Y.; Petta, J. R.; Ambily, S.; Shen, Y.; Ralph, D. C.; Malliaras, G. G. *Adv. Mater.* **2003**, *15*, 1632.
- (7) Zaumseil, J.; Someya, T.; Bao, Z.; Loo, Y.-L.; Cirelli, R.; Rogers, J. A. *Appl. Phys. Lett.* **2003**, *82*, 793.
- (8) Collet, J.; Tharaud, O.; Chapoton, A.; Vuillaume, D. *Appl. Phys. Lett.* **2000**, *76*, 1941.
- (9) Komoda, T.; Kita, K.; Kyuno, K.; Toriumi, A. *Jpn. J. Appl. Phys., Part 1* **2003**, *42*, 3662.
- (10) Pinto, N. J.; Johnson, A. T., Jr.; MacDiarmid, A. G.; Mueller, C. H.; Theofylaktos, N.; Robinson, D. C.; Miranda, F. A. *Appl. Phys. Lett.* **2003**, *83*, 4244.
- (11) Zhou, Y.; Freitag, M.; Hone, J.; Staii, C.; Johnson, A. T., Jr.; Pinto, N. J.; MacDiarmid, A. G. *Appl. Phys. Lett.* **2003**, *83*, 3800.
- (12) Long, Y.; Chen, Z.; Wang, N.; Ma, Y.; Zhang, Z.; Zhang, L.; Wan, M. *Appl. Phys. Lett.* **2003**, *83*, 1863.
- (13) Park, J. G.; Kim, G. T.; Krstic, V.; Kim, B.; Lee, S. H.; Roth, S.; Burghard, M.; Park, Y. W. *Synth. Met.* **2001**, *119*, 53.
- (14) Bjornholm, T.; Hassenkam, T.; Greve, D. R.; McCullough, R. D.; Jayaraman, M.; Savoy, S. M.; Jones, C. E.; McDevitt, J. T. *Adv. Mater.* **1999**, *11*, 1218.
- (15) Ihn, K. J.; Moulton, J.; Smith, P. J. *Polym. Sci., Part B: Polym. Phys.* **1993**, *31*, 735.
- (16) Mardalen, J.; Samuelsen, E. J.; Pedersen, A. O. *Synth. Met.* **1993**, *55*, 378.
- (17) Kiriy, N.; Jahne, E.; Adler, H.-J.; Schneider, M.; Kiriy, A.; Gorodyska, G.; Minko, S.; Jehnichen, D.; Simon, P.; Fokin, A. A.; Stamm, M. *Nano Lett.* **2003**, *3*, 707.
- (18) Kiriy, N.; Jahne, E.; Kiriy, A.; Adler, H.-J. *Macromol. Symp.* **2004**, *210*, 359.
- (19) Yang, H.; Park, S.; Kim, D.; Oh, K.; Magonov, S.; Cho, K.; Chang, T.; Bao, Z.; Ryu, C. Y. *Polym. Prepr.* **2003**, *44*, 333.
- (20) Yang, H.; Shin, T. J.; Yang, L.; Bao, Z.; Ryu, C. Y.; Cho, K. *Polym. Prepr.* **2004**, *45*, 212.
- (21) Prosa, T. J.; Winokur, M. J.; Moulton, J.; Smith, P.; Heeger, A. J. *Macromolecules* **1992**, *25*, 4364.
- (22) McCullough, R. D.; Tristram-Nagle, S.; Williams, S. P.; Lowe, R. D.; Jayaraman, M. *J. Am. Chem. Soc.* **1993**, *115*, 4910.
- (23) Kline, R. J.; McGehee, M. D.; Kadnikova, E. N.; Liu, J.; Frechet, J. M. J. *Adv. Mater.* **2003**, *15*, 1519.
- (24) Hugger, S.; Thomann, R.; Heinzl, T.; Thurn-Albrecht, T. *Colloid Polym. Sci.* **2004**, *282*, 932.
- (25) Seshadri, K.; Frisbie, C. D. *Appl. Phys. Lett.* **2001**, *78*, 993.
- (26) Puntambekar, K. P.; Pesavento, P. V.; Frisbie, C. D. *Appl. Phys. Lett.* **2003**, *83*, 5539.
- (27) Burgi, L.; Richards, T. J.; Friend, R. H.; Sirringhaus, H. *J. Appl. Phys.* **2003**, *94*, 6129.
- (28) Necludov, P. V.; Shur, M. S.; Gundlach, D. J.; Jackson, T. N. *Solid-State Electron.* **2003**, *47*, 259.
- (29) Klauk, H.; Schmid, G.; Radlik, W.; Weber, W.; Zhou, L.; Sheraw, C. D.; Nichols, J. A.; Jackson, T. N. *Solid-State Electron.* **2003**, *47*, 297.

- (30) Deshmukh, M. M.; Ralph, D. C.; Thomas, M.; Silcox, J. *Appl. Phys. Lett.* **1999**, *75*, 1631.
- (31) Verlaak, S.; De Jonge, S.; Noppe, S.; Janssen, D.; Steudel, S.; De Vusser, S.; Heremans, P. *Mater. Res. Soc. Symp. Proc.* **2003**, *771*, 181.
- (32) Ono, K.; Shimada, H.; Kobayashi, S.-i.; Ootuka, Y. *Jpn. J. Appl. Phys., Part 1* **1996**, *35*, 2369.
- (33) Brugger, J.; Berenschot, J. W.; Kuiper, S.; Nijdam, W.; Otter, B.; Elwenspoek, M. *Microelectron. Eng.* **2000**, *53*, 403.
- (34) Kohler, J.; Albrecht, M.; Musil, C. R.; Bucher, E. *Physica E* **1999**, *4*, 196.
- (35) Zhou, Y. X.; Johnson, A. T., Jr.; Hone, J.; Smith, W. F. *Nano Lett.* **2003**, *3*, 1371.
- (36) Amar, A.; Lozes, R. L.; Sasaki, Y.; Davis, J. C.; Packard, R. E. *J. Vac. Sci. Technol., B* **1993**, *11*, 259.
- (37) Rooks, M. J.; Tiberio, R. C.; Chapman, M.; Hammond, T.; Smith, E.; Lenef, A.; Rubenstein, R.; Pritchard, D.; Adams, S. *J. Vac. Sci. Technol., B* **1995**, *13*, 2745.
- (38) Ralls, K. S.; Buhrman, R. A.; Tiberio, R. C. *Appl. Phys. Lett.* **1989**, *55*, 2459.
- (39) Merlo, J. A.; Frisbie, C. D. *J. Polym. Sci., Part B: Polym. Phys.* **2003**, *41*, 2674.
- (40) Trznadel, M.; Pron, A.; Zagorska, M.; Chrzaszcz, R.; Pielichowski, J. *Macromolecules* **1998**, *31*, 5051.
- (41) Liu, J.; Loewe, R. S.; McCullough, R. D. *Macromolecules* **1999**, *32*, 5777.
- (42) Grevin, B.; Rannou, P.; Payerne, R.; Pron, A.; Travers, J. P. *J. Chem. Phys.* **2003**, *118*, 7097.
- (43) Montaudo, G.; Montaudo, M. S.; Puglisi, C.; Samperi, F. *Rapid Commun. Mass Spectrom.* **1995**, *9*, 453.
- (44) Axelsson, J.; Scrivener, E.; Haddleton, D. M.; Derrick, P. J. *Macromolecules* **1996**, *29*, 8875.
- (45) Schriemer, D. C.; Li, L. *Anal. Chem.* **1997**, *69*, 4176.
- (46) Schriemer, D. C.; Li, L. *Anal. Chem.* **1997**, *69*, 4169.
- (47) Erwin, M. M.; McBride, J.; Kadavanich, A. V.; Rosenthal, S. J. *Thin Solid Films* **2002**, *409*, 198.
- (48) Kokubo, H.; Yamamoto, T.; Kondo, H.; Akiyama, Y.; Fujimura, I. *Jpn. J. Appl. Phys., Part 1* **2003**, *42*, 6627.
- (49) Holdcroft, S. *J. Polym. Sci., Part B: Polym. Phys.* **1991**, *29*, 1585.
- (50) Raja, M.; Lloyd, G. C. R.; Sedghi, N.; Eccleston, W.; Lucrezia, R. D.; Higgins, S. J. *J. Appl. Phys.* **2002**, *92*, 1441.
- (51) Raja, M.; Lloyd, G.; Sedghi, N.; di Lucrezia, R.; Higgins, S. J.; Eccleston, W. *Mater. Res. Soc. Symp. Proc.* **2002**, *708*, 423.
- (52) Mas-Torrent, M.; Den Boer, D.; Durkut, M.; Hadley, P.; Schenning, A. P. H. J. *Nanotechnology* **2004**, *15*, S265.
- (53) Volkel, A. R.; Street, R. A.; Knipp, D. *Phys. Rev. B: Condens. Matter* **2002**, *66*, 195336.
- (54) Podzorov, V.; Sysoev, S. E.; Loginova, E.; Pudalov, V. M.; Gershenson, M. E. *Appl. Phys. Lett.* **2003**, *83*, 3504.
- (55) Podzorov, V.; Pudalov, V. M.; Gershenson, M. E. *Appl. Phys. Lett.* **2003**, *82*, 1739.
- (56) Takeya, J.; Goldmann, C.; Haas, S.; Pernstich, K. P.; Ketterer, B.; Batlogg, B. *J. Appl. Phys.* **2003**, *94*, 5800.
- (57) Yagi, I.; Tsukagoshi, K.; Aoyagi, Y. *Appl. Phys. Lett.* **2004**, *84*, 813.
- (58) Chesterfield, R. J.; McKeen, J. C.; Newman, C. R.; Frisbie, C. D.; Ewbank, P. C.; Mann, K. R.; Miller, L. L. *J. Appl. Phys.* **2004**, *95*, 6396.
- (59) Hattori, R.; Kanicki, J. *Jpn. J. Appl. Phys., Part 2* **2003**, *42*, 907.
- (60) Chiang, C.-S.; Chen, C.-Y.; Kanicki, J. *IEEE Electron Device Lett.* **1998**, *19*, 382.
- (61) Liu, S.-D.; Shih, A.; Chen, S.-D.; Lee, S.-C. *J. Vac. Sci. Technol., B* **2003**, *21*, 677.
- (62) Chen, C.-Y.; Kanicki, J. *IEEE Electron Device Lett.* **1997**, *18*, 340.
- (63) Burgi, L.; Sirringhaus, H.; Friend, R. H. *Appl. Phys. Lett.* **2002**, *80*, 2913.
- (64) Sirringhaus, H.; Tessler, N.; Thomas, D. S.; Brown, P. J.; Friend, R. H. *Adv. Solid State Phys.* **1999**, *39*, 101.
- (65) Meijer, E. J.; Gelinck, G. H.; Van Veenendaal, E.; Huisman, B. H.; De Leeuw, D. M.; Klapwijk, T. M. *Appl. Phys. Lett.* **2003**, *82*, 4576.
- (66) Bao, Z.; Dodabalapur, A.; Lovinger, A. J. *Appl. Phys. Lett.* **1996**, *69*, 4108.
- (67) Ukai, S.; Ito, H.; Kuroda, S.-i. *Jpn. J. Appl. Phys., Part 1* **2004**, *43*, 366.
- (68) Rep, D. B. A.; Huisman, B. H.; Meijer, E. J.; Prins, P.; Klapwijk, T. M. *Mater. Res. Soc. Symp. Proc.* **2001**, *660*, JJ7.9.1.
- (69) Sirringhaus, H.; Tessler, N.; Friend, R. H. *Science* **1998**, *280*, 1741.
- (70) Alternatively, the positive V_0 values could be due to an interface dipole rather than acceptor-like states.
- (71) Nikitenko, V. R.; Heil, H.; von Seggern, H. *J. Appl. Phys.* **2003**, *94*, 2480.
- (72) Arkhipov, V. I.; Heremans, P.; Emelianova, E. V.; Adriaenssens, G. J.; Bassler, H. *Appl. Phys. Lett.* **2003**, *82*, 3245.
- (73) Salleo, A.; Chen, T. W.; Voelkel, A. R.; Wu, Y.; Liu, P.; Ong, B. S.; Street, R. A. *Phys. Rev. B: Condensed Matter* **2004**, *70*, 115311.
- (74) Horowitz, G.; Hajlaoui, R.; Delannoy, P. *J. Phys. III* **1995**, *5*, 355.
- (75) Vissenberg, M. C. J. M.; Matters, M. *Phys. Rev. B: Condens. Matter* **1998**, *57*, 12964.
- (76) Mott, N. F.; Davis, E. A. *Electronic Processes in Non-Crystalline Materials*, 2nd ed.; Clarendon Press: Oxford, U. K., 1979.
- (77) Baranovskii, S. D.; Faber, T.; Hensel, F.; Thomas, P. *J. Phys.: Condens. Matter* **1997**, *9*, 2699.
- (78) Monroe, D. *Phys. Rev. Lett.* **1985**, *54*, 146.
- (79) Meijer, E. J.; Tanase, C.; Blom, P. W. M.; van Veenendaal, E.; Huisman, B.-H.; de Leeuw, D. M.; Klapwijk, T. M. *Appl. Phys. Lett.* **2002**, *80*, 3838.
- (80) Sirringhaus, H.; Brown, P. J.; Friend, R. H.; Nielsen, M. M.; Bechgaard, K.; Langeveld-Voss, B. M. W.; Spiering, A. J. H.; Janssen, R. A. J.; Meijer, E. W.; Herwig, P.; De Leeuw, D. M. *Nature* **1999**, *401*, 685.
- (81) Meijer, E. J.; Matters, M.; Herwig, P. T.; de Leeuw, D. M.; Klapwijk, T. M. *Appl. Phys. Lett.* **2000**, *76*, 3433.
- (82) Le Comber, P. G.; Spear, W. E. *Phys. Rev. Lett.* **1970**, *25*, 509.